



PAPER

[View Article Online](#)
[View Journal](#) | [View Issue](#)

 Cite this: *Energy Environ. Sci.*, 2024, 17, 1984

Modulating the electronic structure of Ni(OH)₂ by coupling with low-content Pt for boosting the urea oxidation reaction enables significantly promoted energy-saving hydrogen production†

 Mengxiao Zhong,^a Meijiao Xu,^a Siyu Ren,^a Weimo Li,^a Ce Wang,^a ^a Mingbin Gao^{*b} and Xiaofeng Lu ^{*a}

Replacing the high-potential oxygen evolution reaction (OER) by the low-potential nucleophile oxidation reaction (NOR) is an essential way to further promote the production rate of hydrogen during water electrolysis. Here, low-content Pt-anchored Ni(OH)₂ on the surface of nickel-carbon nanofibers (Ni-CNFs) are prepared via a simple electrospinning–electrodeposition strategy to achieve the alkaline urea oxidation reaction (UOR) electrocatalysis, and they are optimized by controlling different concentrations of deposition solutions during the electrodeposition process. Owing to the Pt loading on the Ni(OH)₂ surface, the dehydrogenation processes of both Ni(OH)₂ to Ni(OH)O and urea molecules to N₂ and CO₂ are promoted, leading to a greatly enhanced UOR performance with low potentials of 1.363 and 1.422 V vs. RHE at current densities of 10 and 100 mA cm^{−2} for the optimized Pt–Ni(OH)₂@Ni-CNFs-2 catalyst, which is significantly better than many reported representative Ni-based catalysts. Moreover, considering the superior hydrogen evolution reaction (HER) activity of the optimized Pt@Ni-CNFs-2 catalyst through a similar synthetic procedure, a home-made urea-assisted water splitting device is constructed with the Pt–Ni(OH)₂@Ni-CNFs-2 and Pt@Ni-CNFs-2 catalysts serving as the anode and cathode, respectively, which exhibits a voltage of 1.40 V at 10 mA cm^{−2}, surpassing many reported representative urea-assisted water splitting electrolyzers. The as-fabricated electrolyzer displays a significantly promoted H₂ production rate of 10-fold that of the overall water splitting, demonstrating the prominent prospects of our catalysts in urea-assisted water splitting for energy-saving H₂ generation.

 Received 9th October 2023,
 Accepted 26th January 2024

DOI: 10.1039/d3ee03398h

rsc.li/ees

Broader context

Hydrogen has been considered an ideal energy carrier because of its favorable gravimetric energy density, zero contamination and exceptional recyclability. Therefore, the green and environmentally friendly strategy of electrocatalytic overall water splitting has attracted much attention in the field of hydrogen generation. However, the anodic oxygen evolution reaction (OER) of overall water splitting is critical for efficiently utilizing renewable energy resources due to the sluggish kinetics, which greatly hinders the efficiency of hydrogen production. Replacing the high-potential OER process by the low-potential nucleophile oxidation reaction (NOR) is a novel approach to achieve energy-saving hydrogen production. Urea has been proposed as a hydrogen source because of the high gravimetric hydrogen content of 6.71%. In addition, urea has the characteristics of low cost, non-toxic and stable chemical properties, which are widely derived from human/animal urine and industrial production. Thus, replacing OER by the urea oxidation reaction (UOR) during water splitting can not only reduce the energy consumption of hydrogen generation but also treat the urea-rich wastewater. In this work, we demonstrate a Pt-anchored Ni(OH)₂ surface to facilitate the capture of urea and further enhance the hydrogen production rate, which also provides a low-cost and suitable approach for energy-saving hydrogen production.

^a Alan G. MacDiarmid Institute, College of Chemistry, Jilin University, 2699 Qianjin Street, Changchun 130012, P. R. China. E-mail: xflu@jlu.edu.cn

^b National Engineering Research Center of Lower-Carbon Catalysis Technology, Dalian National Laboratory for Clean Energy, Dalian Institute of Chemical Physics, Chinese Academy of Sciences, Dalian 116023, P. R. China. E-mail: mbgao@dicp.ac.cn

† Electronic supplementary information (ESI) available. See DOI: <https://doi.org/10.1039/d3ee03398h>

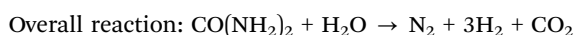
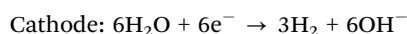
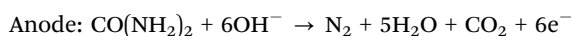
Introduction

With the rising demand for energy and increasing environmental concerns, there exists an urgent need for eco-friendly renewable energy sources to alleviate the consumption of fossil fuels.^{1–4} Hydrogen (H₂) is frequently proposed as a prominent energy carrier because of its favorable gravimetric energy

density, zero contamination and exceptional recyclability.⁵ However, several strategies for producing H₂, such as coal gasification and steam methane reforming, suffer from the drawbacks of low H₂ purity, high energy consumption and unsatisfactory efficiency.⁶ Thus promising approaches for generating H₂ have been proposed, such as electrocatalytic water splitting,⁷ photoelectrochemical (PEC) water splitting,^{8,9} and so on. In line with the goal of sustainable development, electrocatalytic water splitting has garnered substantial attention for its highly efficient H₂ production that is both economical and pollution-free.¹⁰ The process of overall water splitting involves the cathodic hydrogen evolution reaction (HER) and the anodic oxygen evolution reaction (OER), which requires a high thermodynamic voltage of 1.23 V.^{11,12} Nevertheless, the actual operating voltage for water splitting is usually much higher due to the limitation of the sluggish kinetics of the OER.¹¹ To minimize the overpotential during water splitting, the rational design of advanced electrocatalysts for boosting HER and OER activity is an essential approach for enhancing the efficiency of H₂ generation.

In addition to developing highly efficient HER and OER electrocatalysts, it is crucial to replace the anodic OER in overall water splitting by the electrooxidation reaction of small organic molecules for dramatically enhanced energy-saving H₂ production.¹³ Generally, among various kinds of organic molecules, those with nucleophilic groups and active hydrogen are essential to act as substrates for electrooxidation.¹⁴ Thus, the electrooxidation of organic substrates containing hydroxyl, aldehyde and amino groups can be defined as the nucleophile oxidation reaction (NOR), including the urea oxidation reaction (UOR), ethanol oxidation reaction (EOR) and hydrazine oxidation reaction (HzOR), which can be coupled with the HER to reduce the energy consumption in H₂ production.¹⁴ Moreover, the excessive production and use of nitrogen-containing compounds (including urea) can lead to environmental problems such as water eutrophication and disruption of the nitrogen cycle.^{15–17} Hence, the NOR process for the degradation of excessive available nitrogen has gained much attention as an environmentally friendly and gentle alternative for artificially balancing the nitrogen cycle in recent years.

Among these NOR processes, UOR offers great prospects for the replacement of the OER, as it can remarkably reduce the theoretical thermodynamic potential from 1.23 V to 0.37 V.^{18,19} Therefore, the anodic UOR can be coupled with the HER to construct a urea-assisted water splitting configuration in an alkaline environment:



Generally, due to the OH[−]-rich environment of the electrolyte for the UOR, the released CO₂ could react with OH[−] in the electrolyte to form CO₃^{2−} species.^{20,21} Due to the sluggish complex six-electron transfer process, the kinetics of the UOR

is relatively slow, usually resulting in unsatisfactory potentials. Hence, it is crucial and challenging to develop highly efficient UOR catalysts. Urease, which contains nickel sites, is capable of efficiently catalyzing urea.²² Inspired by this natural mechanism, various nickel-based materials, including nickel alloys,^{23,24} nickel oxides,^{25,26} nickel sulfides,^{13,27,28} nickel selenides,²⁹ nickel nitride^{30,31} and nickel hydroxides,³² have been widely considered as prospective candidates for UOR electrocatalysis. The spontaneous transformation of some nickel compounds into Ni–O, and the subsequent combination with adsorbed OH[−] to form Ni(OH)₂, has garnered significant interest because of its structural versatility and the satisfactory availability of 3d electrons.³³ An indirect mechanism for the UOR on the Ni(OH)₂ surface in the alkaline electrolyte has been proposed, revealing that Ni(OH)₂ is firstly electrooxidized to Ni(OH)O in the presence of OH[−] at a higher potential, and thereafter, urea undergoes spontaneous dehydrogenation on the Ni(OH)O surface to form N₂ and CO₂ products, while the catalyst is converted back to Ni(OH)₂.^{14,15} Thus, promoting the electrooxidation from Ni(OH)₂ to Ni(OH)O, and the dehydrogenation of urea molecules on the catalyst surface is vital for the UOR. Modulating the surface electronic structure and promoting the intrinsic activity of accessible active sites through surface engineering are effective strategies to minimize the overpotentials in the electrocatalytic reactions for enhanced performance.^{34,35} It has been reported that the modification of the precious metal with the Ni(OH)₂ catalyst can modify the electronic structure of Ni, optimizing the interaction between the active sites and the intermediates, thus resulting in faster electrocatalytic kinetics for the OER.³⁶ However, there are a few reports to boost the UOR performance by the interfacial engineering of the Ni(OH)₂ catalyst with a precious metal component.

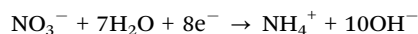
Herein, further inspired by the formation of the Pt–H bond at the active sites to promote the HER performance, we report the fabrication of Pt-anchored Ni(OH)₂ on the surface of nickel-carbon nanofibers (Pt–Ni(OH)₂@Ni-CNFs) and Pt-decorated Ni-CNFs (Pt@Ni-CNFs) *via* a simple electrospinning and electrodeposition technique, which are used as highly efficient UOR and HER electrocatalysts, respectively. Owing to the interfacial interactions between the Pt nanoparticles and Ni(OH)₂, the prepared Pt–Ni(OH)₂@Ni-CNFs catalyst exhibits a prominent UOR performance with low potentials of 1.363 and 1.422 V *vs.* RHE at a current density of 10 and 100 mA cm^{−2} in a 1 M KOH/0.33 M urea system, which is better than many other reported representative UOR electrocatalysts. *In situ* characterizations and density functional theory (DFT) calculations reveal that Pt loading can significantly reduce the energy barrier during the UOR process, further promoting electrocatalytic performance. In addition, the Pt@Ni-CNFs catalyst presents excellent HER performance with an ultralow overpotential of 20.8 mV at a current density of 10 mA cm^{−2} in 1 M KOH, even surpassing that of the benchmark Pt/C catalyst. As a result of the superior UOR and HER performances, a urea-assisted water splitting electrolyzer is assembled, in which Pt–Ni(OH)₂@Ni-CNFs and Pt@Ni-CNFs are served as anodic and cathodic electrodes, respectively. The electrolyzer delivers a low voltage of 1.40 V

at 10 mA cm^{-2} , and presents an enhanced 10-fold H_2 generation rate compared with the overall water splitting device, which illustrates prominent prospects for energy-saving H_2 production.

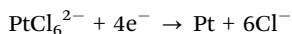
Results and discussion

Fabrication and characterization of catalysts

As illustrated in Fig. 1, the Ni precursor-polyacrylonitrile (PAN) nanofibers are firstly prepared *via* an electrospinning technology with diameters in the range of 490–550 nm (Fig. S1, ESI[†]). Then, after the high temperature carbonization process, the obtained Ni-CNFs membranes significantly shrink to 470–520 nm, which results from the pyrolysis of the polymer (Fig. S2a and b, ESI[†]). Thanks to the soft and flexible nature of the Ni-CNF membranes, they contribute as self-supporting working electrodes for electrodeposition reactions. Based on the standard electrode potential, the reduction of NO_3^- in the $\text{Ni}(\text{NO}_3)_2$ solution is given priority over H_2O and Ni^{2+} on the cathode, which is depicted as follows:



Therefore, Ni^{2+} and OH^- are deposited on the cathode electrode, resulting in the formation of $\text{Ni}(\text{OH})_2$.^{37,38} Meanwhile, PtCl_6^{2-} ions in the solution undergo a reduction process on the cathode:³⁹



We have prepared a range of deposition solutions with varying concentrations for the electrodeposition process, where the deposition solutions for $\text{Ni}(\text{OH})_2@$ Ni-CNFs and $\text{Pt-Ni}(\text{OH})_2@$ Ni-CNFs samples include 20 mL of aqueous solution with 15 mM $\text{Ni}(\text{NO}_3)_2$ and varied concentrations of H_2PtCl_6 (0, 1.25, 2.5 and 3.75 mM). Field emission scanning electron microscopy (FESEM) and transmission electron microscopy (TEM) images reveal that the presence of the Ni precursor in the solution results in the hierarchical nanosheets coating on the fiber surface of Ni-CNFs (Fig. 2a, b and Fig. S2c–h, ESI[†]). Notably, a thicker surface nanosheet-like coating is observed when the Pt content in the deposition solution is low, which may be attributed to the deposition sequence of Ni and Pt species on the cathode. In addition, it is evident that many Ni nanoparticles are evenly embedded throughout the entire nanofibers, contributing to the promotion of the electron

transfer properties. As shown in Fig. 2c, the diffraction peaks of Ni-CNFs sample in the X-ray diffraction (XRD) pattern at 44.6° , 52.1° and 76.5° can be indexed to the (111), (200) and (220) planes of metallic Ni (JCPDS No. 04-0850), which are still maintained after the electrodeposition process. With increasing Pt concentration in the deposition solution, a broad peak appears at 39.8° , corresponding to the (111) plane of metallic Pt (JCPDS No. 04-0802).^{40–42} Although there is no obvious diffraction peak associated with Pt in the XRD pattern of $\text{Pt-Ni}(\text{OH})_2@$ Ni-CNFs-2, the lattice fringe of the surface nanoparticle with a spacing of 0.224 nm in the high-resolution (HRTEM) image ascribes to the (111) plane of metallic Pt (Fig. 2d). Moreover, the distinct flexural lattice fringe of C (002) with a *d*-spacing of 0.360 nm can be observed, indicating the high graphitization of the carbon substrate, which facilitates electron transport.¹⁸ Fig. S3 (ESI[†]) shows the energy dispersive X-ray (EDX) pattern that further confirms the existence of the Pt element. And EDX mappings also present the uniform distribution of Pt, Ni, O and C elements (Fig. 2e and Fig. S4, ESI[†]). To identify the compositions of surface nanosheets, we employ a Pt-free $\text{Ni}(\text{OH})_2@$ Ni-CNFs sample that is prepared in a more concentrated solution as reference, and its XRD pattern shows the diffraction peaks pointing to α - $\text{Ni}(\text{OH})_2$ (JCPDS No. 38-0715) (Fig. S5, ESI[†]). Furthermore, Raman spectra show that the peak located at around 510 cm^{-1} in the Pt-free and $\text{Pt-Ni}(\text{OH})_2@$ Ni-CNFs samples corresponds to the Ni(II)–O bond of $\text{Ni}(\text{OH})_2$ (Fig. 2f), which confirms the formation of $\text{Ni}(\text{OH})_2$.⁴³ Nevertheless, another peak attributed to the Pt–O bond appears at 560 cm^{-1} in the Pt-containing samples, suggesting that the Pt species are attached to $\text{Ni}(\text{OH})_2$.^{44,45} To further analyze the chemical composition of the nanofibers, X-ray photoelectron spectroscopy (XPS) is conducted to depict the surface valence states of the prepared samples. The XPS survey spectrum of $\text{Pt-Ni}(\text{OH})_2@$ Ni-CNFs-2 shows the coexistence of Pt, Ni, C and O elements (Fig. S6a, ESI[†]). In detail, as shown in Fig. 2g, the $\text{Pt-Ni}(\text{OH})_2@$ Ni-CNFs-2 sample exhibits prominent characteristic peaks at binding energies of 71.2 and 74.6 eV, corresponding to $\text{Pt } 4f_{7/2}$ and $4f_{5/2}$ of Pt^0 , respectively.^{40,46,47} Furthermore, the peaks at 72.1 and 75.9 eV are assigned to the high-valence state of $\text{Pt}^{\delta+}$, confirming the successful introduction of the Pt species.^{40,46,47} Notably, the binding energy peaks of Pt 4f and Ni 3p partially overlap, whereas the peak with a binding energy of 68.5 eV corresponds to Ni 3p.⁴⁰ In the Ni 2p spectrum of the $\text{Pt-Ni}(\text{OH})_2@$ Ni-CNFs-2 sample, the characteristic peaks of Ni $2p_{3/2}$ and $2p_{1/2}$ corresponding to Ni^{2+} in $\text{Ni}(\text{OH})_2$ appear at 856.0 and 873.4 eV

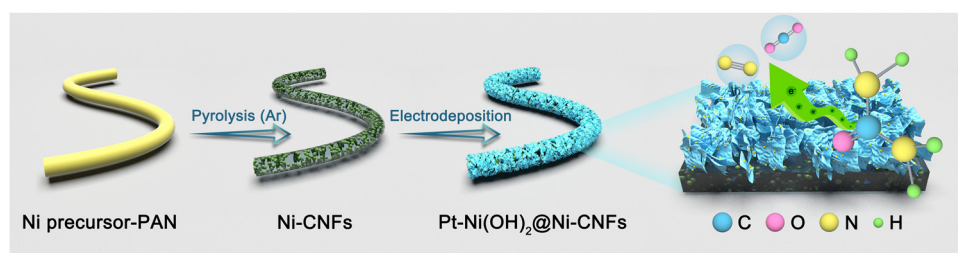


Fig. 1 Schematic diagram of the fabrication of $\text{Pt-Ni}(\text{OH})_2@$ Ni-CNFs.

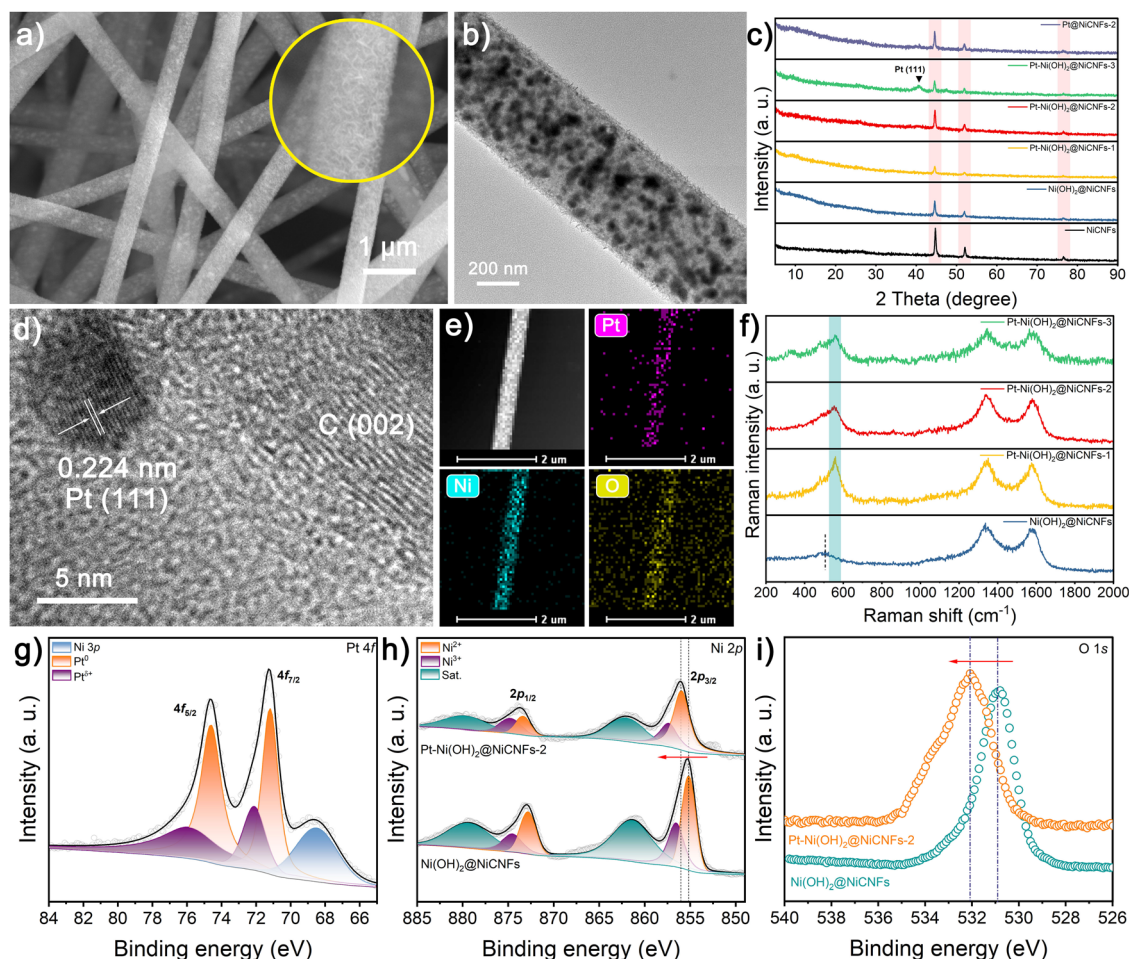


Fig. 2 (a) SEM and (b) TEM images of Pt–Ni(OH)₂@Ni–CNFs–2. (c) XRD patterns of different samples. (d) HRTEM image, (e) HAADF–STEM micrograph and EDX mappings of Pt, Ni and O elements of Pt–Ni(OH)₂@Ni–CNFs–2. (f) Raman spectra of different samples. (g) Narrow-scan XPS spectrum of Pt 4f of Pt–Ni(OH)₂@Ni–CNFs–2. Narrow-scan (h) Ni 2p and (i) O 1s XPS spectra of Pt–Ni(OH)₂@Ni–CNFs–2 and Ni(OH)₂@Ni–CNFs.

(Fig. 2h).⁴⁸ Compared with the Ni(OH)₂@Ni–CNFs sample without Pt loading, there is an obvious positive shift of the Ni 2p peaks, implying that the introduction of Pt changes the electron density around the Ni atom, and thereby improves the electrocatalytic oxidative activity.^{36,49} In addition, the doublets at 857.4 and 874.7 eV belong to the Ni 2p_{3/2} and 2p_{1/2} of Ni³⁺. The characteristic peak in the narrow-scan O 1s spectrum of Pt–Ni(OH)₂@Ni–CNFs–2 shifts in the direction of high binding energy compared to the Pt-free sample, which is mainly due to the formation of the Pt–O bond.^{40,50,51} On the other hand, the noticeable peaks of Pt–Ni(OH)₂@Ni–CNFs at 284.8, 285.8 and 289.1 eV in the C 1s spectrum belong to C–C/C=C, C–O and C=O bonds, respectively, which is originated from the carbon network after PAN carbonization (Fig. S6b, ESI†).

For comparison, Pt@Ni–CNFs samples are also fabricated through a similar electrodeposition process in Ni precursor-free solution. No significant changes are observed in the surface morphology and the diameter of the final nanofibers compared with the neat Ni–CNFs, because the singlet Pt primarily exists in the form of small nanoparticles, which have minimal impact on the changes in surface morphology and fiber diameter (Fig. S7a, b

and S8, ESI†). The XRD pattern shown in Fig. S9 (ESI†) demonstrates that in addition to the intense diffraction peaks of metallic Ni, only the sample with high Pt loading can detect the characteristic peak of metallic Pt(111). However, a lattice spacing of 0.224 nm is still observed in the Pt@Ni–CNFs–2 sample, which is indexed to the (111) plane of metallic Pt (Fig. S7c, ESI†). And the appearance of the Pt signal in the EDX pattern further confirms the successful formation of Pt nanoparticles on Ni–CNFs (Fig. S7d, ESI†). Additionally, the HAADF–STEM micrograph and the corresponding EDX mapping illustrate the uniform distribution of Pt, Ni and C elements (Fig. S7e, ESI†). The XPS survey spectra of Pt@Ni–CNFs–2 and Ni–CNFs show the presence of Ni and C elements in the nanofibers, and a clear characteristic peak of Pt 4f in Pt@Ni–CNFs–2, demonstrating the successful loading of Pt in the Pt@Ni–CNFs–2 sample (Fig. S10a, ESI†). The binding energy peaks of Pt 4f observed in Fig. S10b (ESI†) can be deconvoluted into Pt 4f_{7/2} (71.5 eV) and Pt 4f_{5/2} (74.9 eV) for metallic Pt, and Pt 4f_{7/2} (72.5 eV) and Pt 4f_{5/2} (76.0 eV) for Pt^{δ+}, where the binding energy peak located at 68.1 eV corresponds to Ni 3p. In the Ni 2p narrow-scan spectrum of Pt@Ni–CNFs–2, two typical peaks at 853.2 and 870.6 eV correspond to Ni 2p_{3/2} and 2p_{1/2} of metallic

Ni, respectively (Fig. S10c, ESI†). Moreover, the noticeable peaks located at 856.2 and 874.1 eV are attributed to Ni 2p_{3/2} and 2p_{1/2} of Ni²⁺ derived from the surface oxidation, and they are accompanied by a pair of satellite peaks. It is noteworthy that the characteristic peaks of metallic Ni in Pt@Ni-CNFs-2 illustrate a negative shift compared with the Pt-free Ni-CNF sample, demonstrating that Pt loading modulates the electron density of Ni sites. Finally, the narrow-scan C 1s spectrum in Fig. S10d (ESI†) can also be fitted to C-C/C=C (284.8 eV), C-O (285.6 eV) and C=O (288.5 eV). The mass loading of Pt and Ni in catalysts is further determined by inductively coupled plasma optical emission spectroscopy (ICP-OES) measurement, in which the Pt-Ni(OH)₂@Ni-CNFs-2 and Pt@Ni-CNFs-2 contain only 6.1 and 6.5 wt% metallic Pt, respectively (Table S1, ESI†).

UOR performance in a three-electrode configuration

The UOR performance of the as-prepared varied catalysts is assessed by a simple three-electrode system. As shown in

Fig. 3a, the linear sweep voltammetry (LSV) curve of Pt-Ni(OH)₂@Ni-CNFs-2 toward the UOR exhibits a potential advantage of 274 mV over the OER at a current density of 50 mA cm⁻², indicating that the UOR catalysis is more favorable and energy-efficient than the OER based on the fabricated Pt-Ni(OH)₂@Ni-CNFs-2 catalyst. In addition, the oxidation peak at a potential of 1.36 V vs. RHE in the LSV curve of the OER corresponds to the Ni²⁺/Ni³⁺ redox couple in the anodic potential range for most nickel-based catalysts, which approximates the onset potential of the UOR. This suggests that UOR catalysis may also be related to the electrochemical oxidation of the nickel active site. The cyclic voltammetry (CV) curves for the UOR at different scan rates are obtained with reduction peaks corresponding to the reduction process of Ni²⁺/Ni³⁺ redox pairs, and the reduction peak current density is plotted *versus* the square root of the scan rate, which shows a good linear relationship as a function, indicating that the redox of Ni²⁺/Ni³⁺ is a diffusion-controlled process (Fig. S11, ESI†).⁵⁴ Moreover,

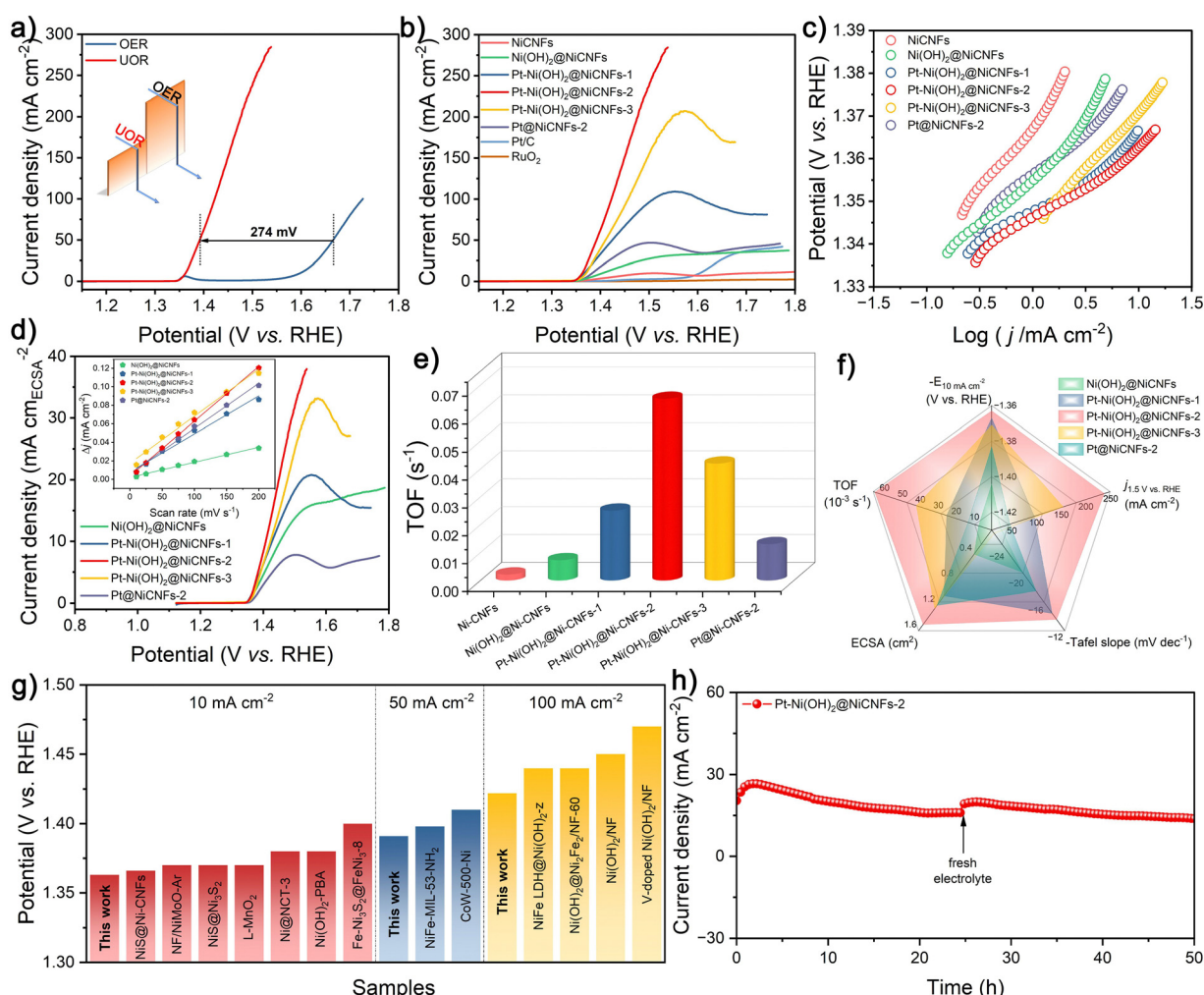


Fig. 3 (a) Polarization curves of Pt-Ni(OH)₂@Ni-CNFs-2 for the UOR and OER in 1 M KOH/0.33 M urea and 1 M KOH, respectively. (b) Polarization curves and (c) corresponding Tafel plots of different catalysts. (d) ECSA-normalized polarization curves and (d, inset) capacitive current density of different catalysts with linear fitting with different scan rates of different catalysts. (e) Comparison of TOF values of different control catalysts. (f) Comprehensive performance comparison of different catalysts. (g) Comparison of some representative catalysts for UOR activity. (h) *i*-*t* curve of Pt-Ni(OH)₂@Ni-CNFs-2 for the UOR at a potential of 0.47 V vs. Hg/HgO.

the much lower Tafel slope of the UOR (13.7 mV dec^{-1}) compared with the OER (84.8 mV dec^{-1}) further confirms the faster kinetics of the UOR process for the fabricated Pt-Ni(OH)₂@Ni-CNFs-2 catalyst (Fig. S12, ESI†). In the following, the impact of the electrolyte concentration on the UOR activity has been investigated. As shown in Fig. S13a (ESI†), the polarization curves of Pt-Ni(OH)₂@Ni-CNFs-2 in 1 M KOH electrolyte containing different concentrations of urea reveal that the current density increases gradually in the low concentration range and reaches the maximum value at 0.33 M urea concentration. In the electrolyte with a high concentration of urea, the surface of Pt-Ni(OH)₂@Ni-CNFs-2 is heavily covered by urea molecules and catalytic intermediates, which hampers the contact of OH[−] species with the active sites, thereby reducing the urea oxidation rate.^{55,56} In addition, excess urea undergoes hydrolysis to generate CO₂, which in turn mitigates the current density.⁵⁵ As a result, a concentration of 0.33 M urea is used in the UOR process to attain the maximum current density, which is also equivalent to the concentration of urea in human urine. On the other hand, the UOR performance of the catalyst is also explored by the LSV method in the KOH system with varied concentrations (Fig. S13b, ESI†). The onset potential shifts towards the negative range with increasing KOH concentration, indicating that higher KOH concentrations can stimulate the formation of active species.⁵⁷ Similarly, the anodic current density increases with KOH concentration, which is mainly due to the increased electrolyte conductivity, thereby facilitating current transport. However, a substantial reduction in current density is observed at high potentials when the KOH concentration reaches 6 M, which is likely attributed to the complete coverage of OH[−] on the surface of the electrocatalyst, hindering the contact between urea molecules and the electrode to yield decreased activity.^{55,56} Thus, the subsequent UOR experiments are performed employing the 1 M KOH/0.33 M urea system.

For further comparison, the UOR activities of other control samples are explored. As shown in Fig. 3b, the Ni(OH)₂@Ni-CNFs catalyst requires 1.404 V *vs.* RHE to attain a current density of 10 mA cm^{-2} . However, it is observed that the current densities of Pt-Ni(OH)₂@Ni-CNFs catalysts are dramatically enhanced upon the addition of Pt solution to the electrodeposition system; among them, the Pt-Ni(OH)₂@Ni-CNFs-2 catalyst only requires 1.363 V *vs.* RHE to drive a current density of 10 mA cm^{-2} , which surpasses those of Pt-Ni(OH)₂@Ni-CNFs-1 (1.367 V *vs.* RHE) and Pt-Ni(OH)₂@Ni-CNFs-3 (1.371 V *vs.* RHE). Moreover, the polarization curve of the sample with individual electrodeposited Pt nanoparticles (Pt@Ni-CNFs-2) presents a potential of 1.383 V *vs.* RHE at a current density of 10 mA cm^{-2} . It can be seen that the UOR performances of both Ni(OH)₂@Ni-CNFs and Pt@Ni-CNFs-2 are lower than those of the Pt-Ni(OH)₂@Ni-CNF samples, suggesting that the excellent electrocatalytic UOR performance of our prepared catalyst is due to the mutual synergistic effect between surface Pt nanoparticles and Ni(OH)₂.

Additionally, the Pt-Ni(OH)₂@Ni-CNFs-2 catalyst presents a current density of 238.4 mA cm^{-2} at 1.5 V *vs.* RHE, which

displays a significant enhancement compared with the Pt-free Ni(OH)₂@Ni-CNFs catalyst (27.5 mA cm^{-2}). The Tafel slope of Pt-Ni(OH)₂@Ni-CNFs-2 for the UOR process is calculated as 13.7 mV dec^{-1} , which is lower than those of Pt-Ni(OH)₂@Ni-CNFs-1 (14.6 mV dec^{-1}), Pt-Ni(OH)₂@Ni-CNFs-3 (26.5 mV dec^{-1}), Ni(OH)₂@Ni-CNFs (20.7 mV dec^{-1}), Pt-Ni-CNFs-2 (17.9 mV dec^{-1}) and Ni-CNFs (26.2 mV dec^{-1}), suggesting the enhanced reaction kinetics of Pt-Ni(OH)₂@Ni-CNFs-2 for the UOR (Fig. 3c). The kinetics of this catalyst for the UOR can be further investigated *via* EIS measurements. According to the Nyquist plot illustrated in Fig. S14 (ESI†), the Pt-NiS@Ni-CNFs-2.5 catalyst displays the smallest semicircle among all the prepared catalysts, signifying the lowest charge transfer resistance (R_{ct}).

The lower R_{ct} value represents a faster charge transfer capability of the catalysts for improving the electrocatalytic performance. Remarkably, all Pt-loaded catalysts have substantially reduced charge transfer resistance. Based on the previous XPS characterization, it can be inferred that Pt loading modulates electron density at the nickel sites, which promotes electron transfer and enhances the electrocatalytic activity. Furthermore, the electrochemical surface area (ECSA) can be evaluated through the double layer capacitance (C_{dl}) to study the intrinsic activity of catalysts. As depicted in the Fig. S15 (ESI†) and the inset in Fig. 3d, the calculated C_{dl} of Pt-Ni(OH)₂@Ni-CNFs-2 is 0.3 mF cm^{-2} , which is higher than that of Pt-Ni(OH)₂@Ni-CNFs-1 (0.21 mF cm^{-2}), Pt-Ni(OH)₂@Ni-CNFs-3 (0.25 mF cm^{-2}), Ni(OH)₂@Ni-CNFs (0.08 mF cm^{-2}) and Pt@Ni-CNFs-2 (0.24 mF cm^{-2}). In general, the ECSA and roughness factor (RF) can be estimated by C_{dl} , where the higher value of Pt-Ni(OH)₂@Ni-CNFs-2 reveals its more exposed active sites (Table S2, ESI†).^{58,59} Additionally, the ECSA-normalized polarization curves indicate that the Pt-Ni(OH)₂@Ni-CNFs-2 still exceeds other prepared catalysts, indicating its superior intrinsic activity due to the synergistic interaction between Pt and Ni(OH)₂ components (Fig. 3d).⁵⁸ Based on the molar ratio of metal components in the catalysts given in Table S1 (ESI†), the turnover frequency (TOF) values of each catalyst at various potentials are calculated (Fig. 3e and Fig. S16, ESI†). The Pt-Ni(OH)₂@Ni-CNFs-2 possesses the highest TOF of 0.065 s^{-1} at a potential of 1.5 V *vs.* RHE, further demonstrating the faster kinetics and higher intrinsic activity of our prepared catalyst.⁶⁰ The overall performance comparison of the catalysts in Fig. 3f demonstrates that the prepared Pt-Ni(OH)₂@Ni-CNFs-2 has the best electrocatalytic performance for the UOR. Moreover, the prepared Pt-Ni(OH)₂@Ni-CNFs-2 catalyst exhibits excellent activity at different current densities, surpassing many reported representative Ni-based catalysts (Fig. 3g and Table S3, ESI†).^{15,22,48,61–72}

Stability is a critical aspect in assessing the catalyst performance. The long-term *i-t* curve in Fig. 3h exhibits that the Pt-Ni(OH)₂@Ni-CNFs-2 catalyst maintains its electrocatalytic activity in 1 M KOH/0.33 M urea system over 50 h at a continuous current density of 20 mA cm^{-2} , demonstrating its exceptional long-term stability. It is noteworthy that after replacing with the fresh electrolyte, the current density recovers, proving that the current decrease might partially result from the consumption of

urea and the formation of carbonate byproduct from the adsorption of CO_2 in the electrolytic system (Fig. 3h and Fig. S17, ESI†). A series of examinations of $\text{Pt-Ni(OH)}_2\text{@Ni-CNFs-2}$ after the UOR process has been carried out to further understand the origin of the stability (Fig. S18, ESI†). SEM image shows that $\text{Pt-Ni(OH)}_2\text{@Ni-CNFs-2}$ still retains its fibrous morphology and the nanosheet structure, suggesting its structural robustness. The XRD patterns present no significant changes before and after the UOR process. Moreover, XPS analysis confirms the unchanged chemical compositions of the catalyst after the UOR process. The

characteristic peaks in the narrow-scan spectra of Pt 4f and Ni 2p remain consistent with those prior to UOR. In addition, the O 1s spectrum confirms the composition stability of $\text{Pt-Ni(OH)}_2\text{@Ni-CNFs-2}$ with the characteristic peaks corresponding to the metal–O bond, the O–H bond, and the H_2O molecule on the surface of the catalyst, respectively. Notably, the binding energy peak located at 535.7 eV stems from the ether-oxygen bond in Nafion. Furthermore, the ICP results present the low losses of Ni (1.8%) and Pt (6.1%) contents for the $\text{Pt-Ni(OH)}_2\text{@Ni-CNFs-2}$ after the *i-t* test, resulting in its excellent long-term UOR performance.

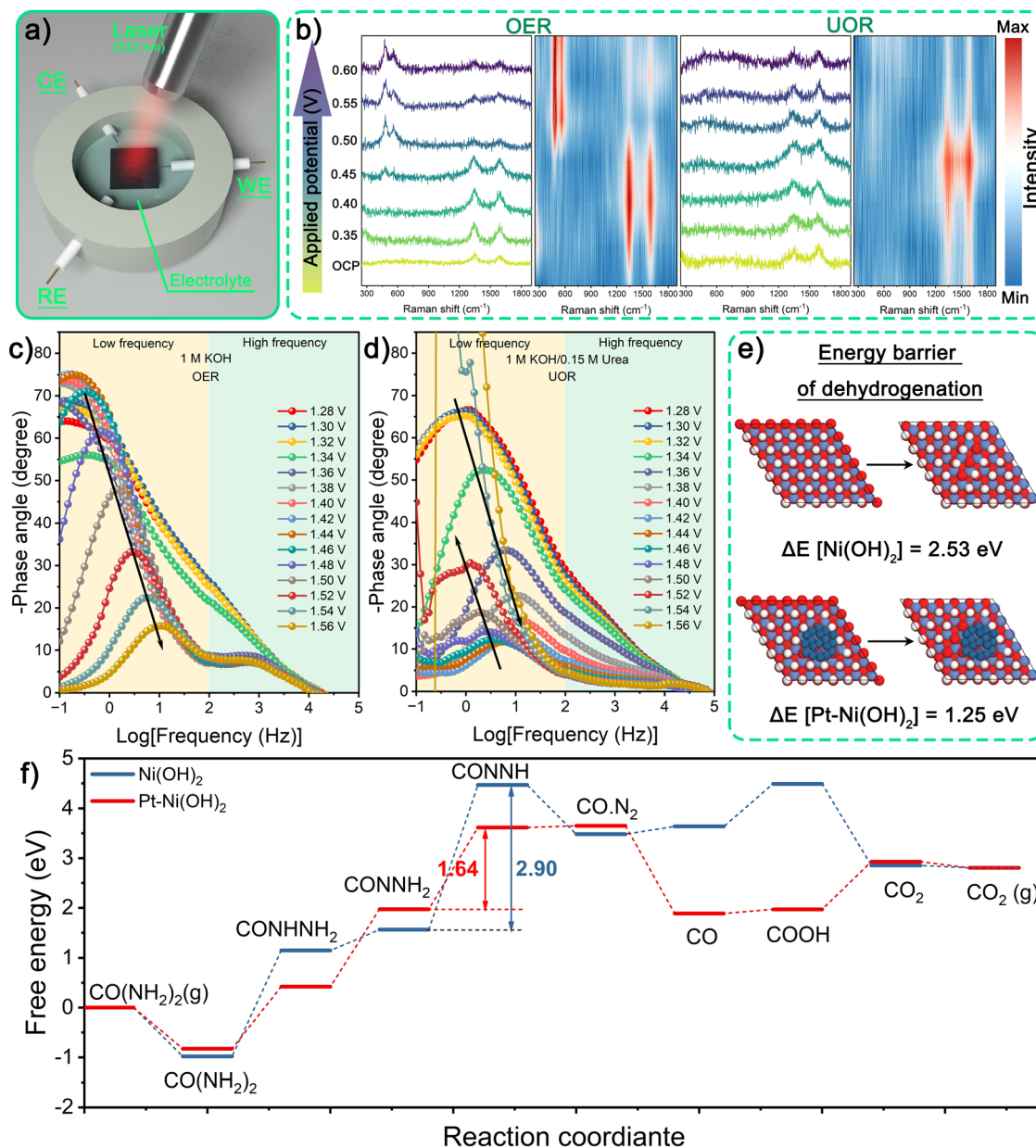


Fig. 4 (a) Schematic diagram of the *in situ* Raman device. (b) *In situ* Raman spectra of $\text{Pt-Ni(OH)}_2\text{@Ni-CNFs-2}$ for the OER and UOR processes. Bode plots of $\text{Pt-Ni(OH)}_2\text{@Ni-CNFs-2}$ at different applied potentials for the (c) OER (1 M KOH) and (d) UOR (1 M KOH/0.15 M urea), respectively. (e) The energy barrier for Ni–OH dehydrogenation at the surface of Ni(OH)_2 and Pt-Ni(OH)_2 catalysts. Here, H, O, Ni and Pt atoms are indicated by white, red, cyan and dark blue spheres, respectively. (f) Calculated Gibbs free energy diagrams for UOR steps on the surface of Ni(OH)_2 and Pt-Ni(OH)_2 catalysts.

Catalytic mechanism for the high UOR performance

It is essential to analyze the phase transition of Pt-Ni(OH)₂@Ni-CNFs-2 during the UOR process to figure out its reaction mechanism. *In situ* Raman spectra are recorded to monitor the change of the chemical structure of the catalyst and its surface species (Fig. 4a). When the applied potential exceeds 0.45 V vs. Hg/HgO (1.372 V vs. RHE) in 1 M KOH for the OER, two distinct Raman peaks appear at 478 and 554 cm⁻¹, which belongs to the Ni³⁺-O bending and stretching vibrations of Ni^{2+δ}O_xH_y species.⁴³ However, these characteristic peaks disappear during the UOR process in the 1 M KOH/0.33 M urea system (Fig. 4b). According to the reported literature, Ni(OH)₂ is usually converted to Ni(OH)O intermediate through the dehydrogenation progress (Ni(OH)₂ + OH⁻ → Ni(OH)O + H₂O + e⁻) under the oxidation potential in an alkaline electrolyte, initially arising at approximately 1.35–1.37 V vs. RHE.¹⁵ Subsequently, the Ni(OH)O intermediates undergo different reactions depending on the electrolyte. In the 1 M KOH electrolyte for the OER process, Ni(OH)O accumulates to form Raman sensitive Ni^{2+δ}O_xH_y species (NiOOH and NiO_x).¹⁴ Conversely, in an electrolyte containing a nucleophile, the generated Ni(OH)O intermediates will be filled with hydrogen from the nucleophile through the spontaneous reduction, thus, leading to their conversion back to Ni(OH)₂, which is difficult to be identified by Raman spectra.^{15,40} Therefore, it can be inferred from the absence of the bending and stretching vibrations of Ni³⁺-O that the accumulation of Ni(OH)O intermediates to Ni^{2+δ}O_xH_y species is inhibited during the UOR process.

To further probe the interface behavior during OER and UOR processes, the electrochemical impedance spectroscopy (EIS) measurement is adopted under diverse potentials. As illustrated in the Bode plots in Fig. 4c, there are two peaks emerging at different frequency ranges when the applied potential exceeds 1.34 V vs. RHE in 1 M KOH. Given the mechanism of alkaline OER on nickel-based catalysts, the peak reflected in the high frequency range is related to the electrocatalytic oxidation of the catalyst (formation of Ni^{2+δ}O_xH_y species), which is associated with the first semicircle in the Nyquist plots (Fig. S19a and b, ESI†). On the other hand, the peak observed in the low frequency range, corresponding to the second semicircle, is indexed to the OER. Beyond the applied potential of 1.46 V vs. RHE, the phase angle in the low frequency range drops gradually, representing the progressive faster electron transfer during the OER process with increasing applied potential. In comparison, Fig. 4d shows the Bode plots from the EIS measurement of the UOR process. Unlike the OER process, the Bode plots of the UOR manifest only one peak in the entire applied frequency range, which corresponds to one semicircle in Nyquist plots (Fig. S19c and d, ESI†), implying the charge transfer process during UOR. Consistent with the *in situ* Raman results, the intervention of urea hinders the accumulation of Ni(OH)O to generate Ni^{2+δ}O_xH_y. Furthermore, the phase angle exhibits a sharp drop with an applied potential exceeding 1.34 V vs. RHE, suggesting a faster charge transfer for the UOR process. Notably, the phase angle starts to rise when the applied potential increases above 1.46 V vs. RHE due to the passive reaction on the surface of the catalyst.^{20,34}

As shown in Fig. 3b, the polarization curves indicate that the bare Pt/C cannot catalyze urea oxidation. Therefore, it is possible that the incorporation of Pt can facilitate the dehydrogenation of Ni(OH)₂ to Ni(OH)O, thereby promoting the UOR. To gain a better understanding of the acceleration of Pt loading for dehydrogenation kinetics, density functional theory (DFT) calculations are performed. First, the energy barrier of the dehydrogenation process (ΔE) of Ni-OH is revealed in Fig. 4e and Fig. S20 (ESI†). Pt-Ni(OH)₂ is found to exhibit a ΔE value of 1.25 eV under Pt-O-Ni-OH coordination conditions, which is lower than the bare Ni(OH)₂ surface (2.53 eV), suggesting that Pt loading favors the dehydrogenation of the Ni(OH)₂ surface to form the vacancies. Pt loading can significantly reduce the dehydrogenation energy barrier in the oxidation progress of Ni(OH)₂, ultimately promoting the thermodynamic behavior of the UOR. Furthermore, to validate the adsorption behavior of urea, the adsorption energies (ΔE_{ads}) of -NH₂ and -C=O groups in urea molecules on the catalyst surface are investigated (Fig. S21, ESI†). Our findings depict that the -NH₂ group has a stronger adsorption ability than the -C=O group on both dehydrogenated Ni(OH)₂ and Pt-Ni(OH)₂ catalysts. Therefore, the Gibbs free energy diagrams for UOR steps on Ni(OH)₂ and Pt-Ni(OH)₂ catalysts are calculated based on the adsorption behavior. As illustrated in Fig. 4f and Fig. S22 (ESI†), the dehydrogenation of *CONNH₂ intermediates is the rate-determining step (RDS) during the entire UOR process. Evidently, the calculated Gibbs free energy change (ΔG) of the RDS on Pt-Ni(OH)₂ is 1.64 eV, which is lower than that on Ni(OH)₂ (2.90 eV). In addition, the results indicate that Pt loading promotes the adsorption of the *CO intermediate while not conducive to the adsorption of N₂, enabling the prompt desorption of N₂, and thus facilitating the formation of *COOH from *CO coupling with OH⁻. These findings suggest that the incorporation of Pt species can manipulate the electronic structure and significantly decrease the energy barrier, ultimately resulting in excellent UOR activity.

HER performance in a three-electrode configuration

Bifunctional catalysts have attracted much attention for the development of efficient H₂ production; the UOR serves as an excellent anodic OER replacement reaction for overall water splitting. Hence, the HER performances of a series of the prepared catalysts are investigated. It is found that the Pt@Ni-CNFs-2 catalyst presents the best HER activity, surpassing Pt-Ni(OH)₂@Ni-CNFs-2 and even the benchmark Pt/C catalyst (Fig. 5a and b). In detail, Pt@Ni-CNFs-2 shows an overpotential of 20.8 and 107.8 mV at current densities of 10 and 200 mA cm⁻², which are lower than those of Pt@Ni-CNFs-1 (26.5 and 142.6 mV), Pt@Ni-CNFs-3 (27.3 and 202.3 mV), Pt-Ni(OH)₂@Ni-CNFs-2 (25.5 and 210.9 mV), Ni-CNFs (213.7 and 424.5 mV) and commercial Pt/C (20.9 and 139.3 mV), suggesting that Pt loading on Ni-CNFs promotes HER activity. Meanwhile, the excellent HER activity of Pt@Ni-CNFs-2 is also better than many reported representative catalysts (Table S4, ESI†). The mass activity (MA) of Pt@Ni-CNFs-2 is calculated and further compared with that of commercial Pt/C based on the

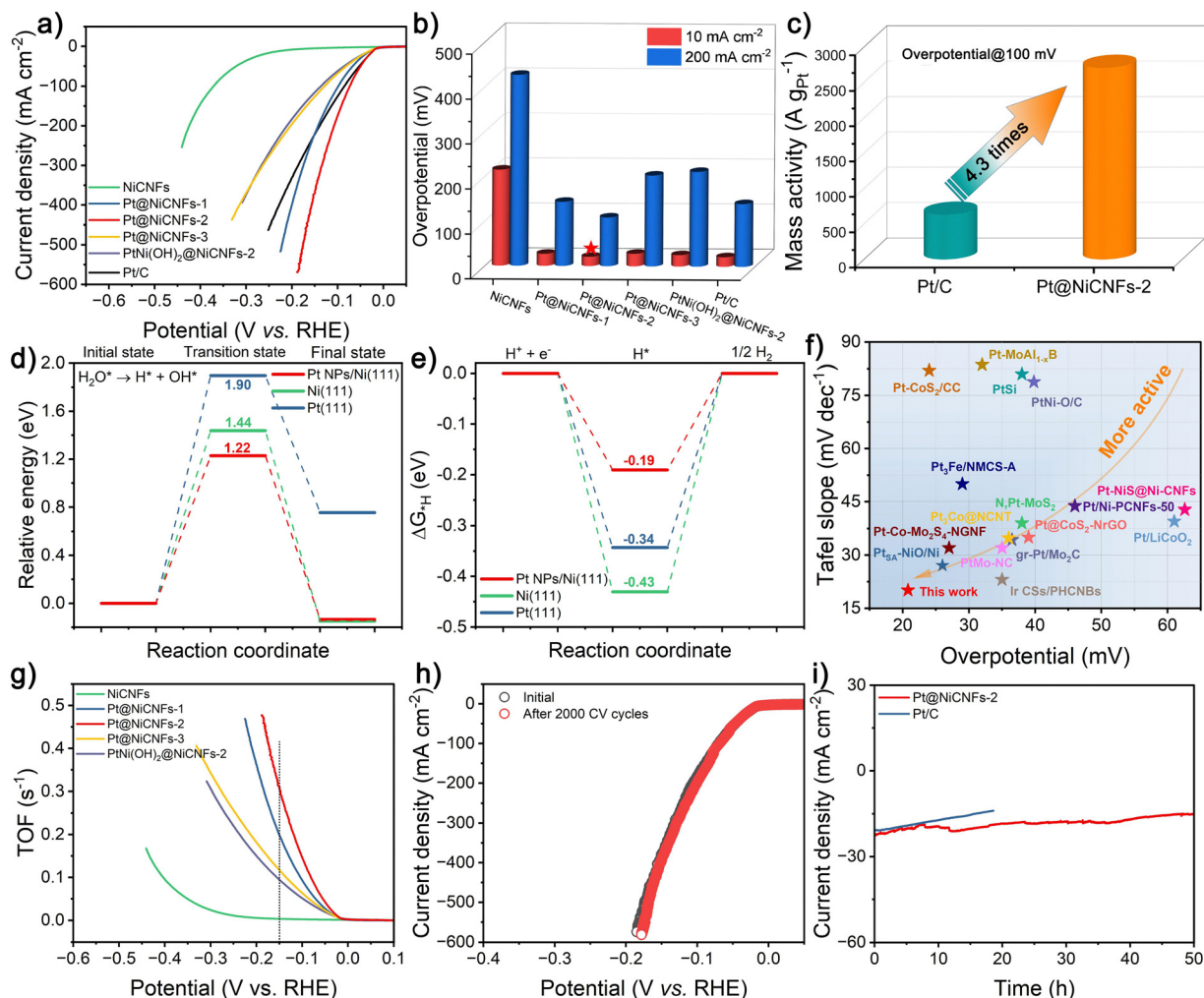


Fig. 5 HER measurements in 1 M KOH. (a) Polarization curves of different catalysts. (b) Overpotentials of different catalysts at 10 and 200 mA cm⁻². (c) Comparison of mass activity of Pt@Ni-CNFs-2 and commercial Pt/C at an overpotential of 100 mV. (d) Calculated free energy diagrams for water dissociation on the surface of Pt(111), Ni(111) and Pt NPs/Ni(111) for the alkaline HER process. (e) Calculated free energy diagrams for hydrogen desorption steps on the surface of Pt(111), Ni(111) and Pt NPs/Ni(111). (f) Comparison of some representative catalysts for HER properties. (g) TOF plots of different catalysts. (h) Polarization curves before and after 2000 CV cycles of Pt@Ni-CNFs-2. (i) *i*-*t* curves of Pt@Ni-CNFs-2 and commercial Pt/C at a potential of -0.97 V vs. Hg/HgO.

Pt content of the sample given in Table S1 (ESI[†]). As shown in Fig. 5c, the MA of Pt@Ni-CNFs-2 at 100 mV is 2706.6 A g⁻¹, which is 4.3-fold that of commercial Pt/C (629.6 A g⁻¹), indicating the realization of low Pt loading of our prepared Pt@Ni-CNFs-2 while still achieving a high activity. This result implies that the excellent HER catalytic activity of Pt@Ni-CNFs-2 may originate not only from the active sites provided by the Pt nanoparticles, but also from the synergistic interaction between Pt nanoparticles and Ni nanoparticles within CNFs (Fig. S7c, ESI[†]), which has been further revealed by DFT calculations. In Fig. 5d and Fig. S23 (ESI[†]), the relatively high water dissociation energy barriers of 1.90 and 1.44 eV on Pt(111) and Ni(111) catalysts can be observed, respectively, demonstrating that Pt(111) and Ni(111) catalysts are inefficient for the water dissociation step under alkaline conditions. However, the activation barriers for water dissociation are remarkably reduced to 1.22 eV on the Pt NPs/Ni(111) catalyst,

indicating the synergistic interaction between the Pt NPs and the Ni surface within CNFs is effective for the cleavage of H-OH bonds. After the formation of *H intermediates in the previous water dissociation step, *H intermediates are desorbed from the metal surface, thus yielding H₂. The calculated hydrogen adsorption free energy value of *H intermediates (ΔG_{H}) of Pt NPs/Ni(111) (-0.19 eV) is higher than that of the Pt(111) surface (-0.34 eV) (Fig. 5e). This suggests that the desorption from *H intermediates to H₂ on Pt NPs/Ni(111) can be faster than that on Pt(111) surface (when $\Delta G_{\text{H}} < 0$, the desorption from *H intermediates to H₂ is the rate-determined step), which can be beneficial for the re-exposure of active sites. This combined with a low energy barrier of water dissociation and fast desorption of *H intermediates on Pt NPs/Ni(111) facilitates highly efficient HER performance under alkaline conditions. The Tafel slope is further evaluated as an important parameter to understand the kinetics of the catalytic reaction (Fig. S24,

ESI†). It is found that Pt@Ni-CNFs-2 has the lowest Tafel slope of 20.1 mV dec^{-1} , lower than those of Pt@Ni-CNFs-1 (24.3 mV dec^{-1}), Pt@Ni-CNFs-3 (20.6 mV dec^{-1}), Ni-CNFs ($150.4 \text{ mV dec}^{-1}$), Pt-Ni(OH)₂@Ni-CNFs-2 (47.4 mV dec^{-1}), and commercial Pt/C (21.3 mV dec^{-1}), demonstrating excellent kinetic merits and superiority over many reported representative HER catalysts (Fig. 5f and Table S4, ESI†). In the HER process, the mechanism of the reaction and its RDS for a catalyst can be approximately estimated based on its Tafel slope. Herein, the Tafel slope of 20.1 mV dec^{-1} for the Pt@Ni-CNFs-2 catalyst suggests its Volmer-Tafel mechanism, with the RDS being the Tafel step ($2\text{H}^* + 2\text{e}^- \rightarrow \text{H}_2$).

The kinetic information of the catalysts for the HER process is further explored by the EIS measurement. As illustrated in Fig. S25 (ESI†), after fitting by equivalent circuit, the R_{ct} of Pt@Ni-CNFs-2 is calculated as 6.07Ω , which is lower than that of other control samples including Pt@Ni-CNFs-1 (6.67Ω), Pt@Ni-CNFs-3 (8.78Ω), Ni-CNFs (494.7Ω) and Pt-Ni(OH)₂@Ni-CNFs-2 (12.41Ω). The smaller R_{ct} value further confirms that Pt@Ni-CNFs-2 possesses faster charge transfer capability and outstanding kinetic advantages, which is beneficial for the synergistic effect between surface Pt nanoparticles and the embedded Ni nanoparticles within CNFs. Moreover, according to the ICP results in Table S1 (ESI†), the TOF plots of the prepared catalysts are obtained by assuming that both Pt and Ni species are participating in the HER catalytic process (Fig. 5g). At an overpotential of 150 mV , the TOF value of the Pt@Ni-CNFs-2 catalyst is 0.311 s^{-1} , which exceeds that of Pt@Ni-CNFs-1 (0.199 s^{-1}), Pt@Ni-CNFs-3 (0.117 s^{-1}), Ni-CNFs (0.003 s^{-1}) and

Pt-Ni(OH)₂@Ni-CNFs-2 (0.095 s^{-1}), indicating the excellent reaction kinetics of the Pt@Ni-CNFs-2 catalyst and its high intrinsic activity. Fig. 5h and 5i illustrate the stability of the Pt@Ni-CNFs-2 catalyst toward the HER in an alkaline system. First, the polarization curves of Pt@Ni-CNFs-2 prior to and post 2000 CV cycles almost overlap, indicating that our prepared catalyst has excellent cycling stability. Second, in the continuous i - t test with a constant applied potential, Pt@Ni-CNFs-2 undergoes an HER progress for 50 h with a slight decline in current density, while the commercial Pt/C decays fast within 20 h, further confirming favorable long-term stability of the Pt@Ni-CNFs-2 catalyst. It brings a promising application prospect in the practical water electrolysis for H₂ production. To gain insight into the structural stability of the Pt@Ni-CNFs-2 catalyst during the HER process, a series of characterizations after i - t testing are performed. As illustrated in Fig. S26a (ESI†), the SEM image of the Pt@Ni-CNFs-2 catalyst post HER shows morphological and structural robustness. In addition, its XRD pattern reveals no obvious phase changes, further realizing the stability of the crystal structure of the Pt@Ni-CNFs-2 catalyst (Fig. S26b, ESI†). The surface chemical valence states of the catalyst post HER process are further investigated through the XPS spectra (Fig. S26c and d, ESI†). Compared with the Ni 2p and Pt 4f spectra of the Pt@Ni-CNFs-2 catalyst before the HER process, neither of them shows significant differences. The ICP results further reveal that Pt loss for the Pt@Ni-CNFs-2 sample (4.6%) is much lower than that of the commercial Pt/C catalyst (22.2%), thus contributing to the better chemical stability of Pt@Ni-CNFs-2 during the HER process.

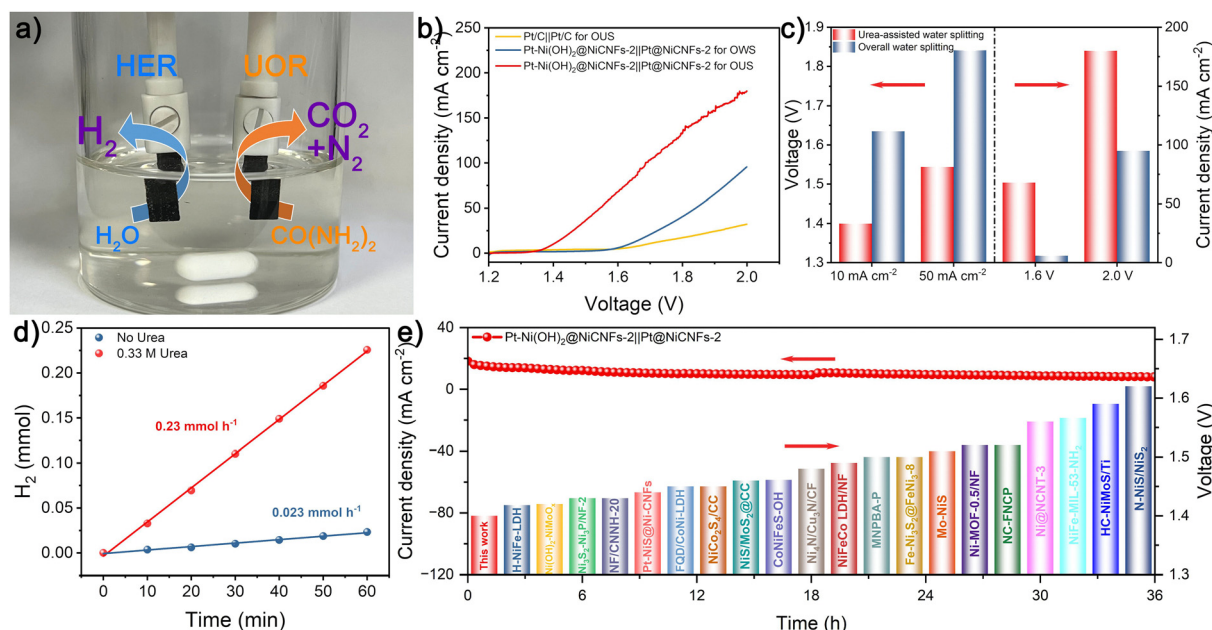


Fig. 6 (a) Digital photograph of the Pt-Ni(OH)₂@Ni-CNFs-2||Pt@Ni-CNFs electrolyzer. (b) Polarization curves of different electrolyzers for overall water splitting and urea-assisted water splitting without iR -compensation. (c) Activity comparison and (d) cathodic H₂ evolution of the Pt-Ni(OH)₂@Ni-CNFs-2||Pt@Ni-CNFs electrolyzer for overall water splitting and urea-assisted water splitting. (e) I - T curve of the Pt-Ni(OH)₂@Ni-CNFs-2||Pt@Ni-CNF electrolyzer at a voltage of 1.44 V , and the comparison of the urea-assisted water splitting activity for Pt-Ni(OH)₂@Ni-CNFs-2||Pt@Ni-CNFs with other reported similar electrolyzers.

Urea-assisted overall water splitting in a two-electrode configuration

In light of the remarkable UOR activity of Pt-Ni(OH)₂@Ni-CNFs-2 and the highly efficient HER performance of Pt@Ni-CNFs-2, a urea-assisted water splitting electrolyzer is assembled in the 1 M KOH/0.33 M urea system with the two catalysts as the anode and cathode, respectively (Fig. 6a). For comparison, an overall water splitting electrolyzer of Pt-Ni(OH)₂@Ni-CNFs-2||Pt@Ni-CNFs-2 is also prepared in 1 M KOH. As illustrated in Fig. 6b and c, the Pt-Ni(OH)₂@Ni-CNFs-2||Pt@Ni-CNFs-2 electrolyzer for overall water splitting requires voltages of 1.635 and 1.841 V to reach the current densities of 10 and 50 mA cm⁻². While for the urea-assisted water splitting with the anodic reaction replaced by the UOR, the same current density can be attained with a voltage of merely 1.400 and 1.544 V. It reveals that replacing the anodic OER process with UOR can achieve the desired current density at a significantly lower voltage, which greatly reduces the energy consumption in the H₂ production process. Consequently, based on the LSV curves of the urea-assisted water splitting and overall water splitting, the power consumptions at different current densities are calculated and presented in Fig. S27 (ESI[†]). The significantly decreased power consumption from 4.27 to 3.58 kW h m⁻³ H₂ at 80 mA cm⁻² can be clearly observed due to the replacement of the OER by the UOR, and it can be concluded that urea-assisted water splitting needs considerably less electrical energy than overall water splitting to achieve the energy-saving hydrogen production.^{73,74}

Therefore, to highlight the advantages of the urea-assisted electrolyzer in practical H₂ production, we have collected the cathodic H₂ from the constructed electrolyzer. The H₂ production rate of 0.23 mmol h⁻¹ is attained at a voltage of 1.60 V for urea-assisted water splitting, which is 10-fold that of overall water splitting without the addition of urea (Fig. 6d). In addition, the urea-assisted water splitting electrolyzer assembled with commercial Pt/C as both the cathode and anode requires a voltage of 1.690 V to attain a current density of 10 mA cm⁻², which is much higher than the Pt-Ni(OH)₂@Ni-CNFs-2||Pt@Ni-CNFs-2 electrolyzer (1.400 V). Furthermore, the cell voltage based on the Pt-Ni(OH)₂@Ni-CNFs-2||Pt@Ni-CNFs-2 electrolyzer for urea-assisted water splitting also outperforms many reported representative electrolyzers at a current density of 10 mA cm⁻² (Fig. 6e and Table S5, ESI[†]). Fig. 6e also presents the stability test of the Pt-Ni(OH)₂@Ni-CNFs-2||Pt@Ni-CNFs-2 electrolyzer at a constant voltage, during which only a slight decline is observed after 36 h, demonstrating its excellent long-term stability.

Conclusions

In summary, we have successfully synthesized highly efficient electrocatalysts for the UOR and HER *via* a simple electrospinning-electrodeposition strategy. The prepared Pt-Ni(OH)₂@Ni-CNFs catalyst only requires a potential of 1.363 and 1.422 V *vs.* RHE to achieve a current density of 10 and

100 mA cm⁻². *In situ* characterization reveals an indirect mechanism on the Pt-Ni(OH)₂@Ni-CNF catalyst toward the UOR, that is, Ni(OH)₂ is firstly electrooxidized to Ni(OH)O followed by the subsequent spontaneous dehydrogenation of the urea molecule at the vacancy site of Ni(OH)O, and then Ni(OH)O is simultaneously converted back to Ni(OH)₂. DFT calculations confirm that Pt loading facilitates the electrooxidation of Ni(OH)₂ and significantly decreases the energy barrier of the RDS, boosting the UOR activity efficiently. On the other hand, the obtained Pt@Ni-CNF catalyst exhibits an extremely higher HER activity than the commercial Pt/C catalyst in an alkaline medium. Therefore, the two-electrode urea-assisted water splitting electrolyzer with Pt-Ni(OH)₂@Ni-CNFs and Pt@Ni-CNFs serving as the anode and cathode, respectively, renders a much lower working voltage in H₂ production compared with the overall water splitting electrolyzer. The H₂ production rate of urea-assisted water splitting is 10-fold that of water splitting, demonstrating the enormous prospective of replacing the OER with UOR in the field of energy-saving and sustainable H₂ production.

Author contributions

Xiaofeng Lu and Ce Wang proposed the idea and supervised the program. Mengxiao Zhong performed the experiments and analyzed the data. Meijiao Xu, Siyu Ren and Weimo Li participated in the data analysis and discussions. Mingbin Gao performed the DFT calculations. Mengxiao Zhong wrote the manuscript and Xiaofeng Lu revised it.

Conflicts of interest

The authors declare that they have no conflict of interest.

Acknowledgements

This work was financially supported by the National Natural Science Foundation of China (52273056) and the Science and Technology Development of Jilin Province, China (20220402008GH). We thank Dr Junyu Yang in Dalian Institute of Chemical Physics, Chinese Academy of Sciences for his help with the DFT calculations on the HER property of Pt@Ni-CNFs.

References

- 1 J. Y. Zhang, H. Wang, Y. Tian, Y. Yan, Q. Xue, T. He, H. Liu, C. Wang, Y. Chen and B. Y. Xia, *Angew. Chem., Int. Ed.*, 2018, **57**, 7649–7653.
- 2 J. Zhu, L. Hu, P. Zhao, L. Y. S. Lee and K. Y. Wong, *Chem. Rev.*, 2020, **120**, 851–918.
- 3 C. McGlade and P. Ekins, *Nature*, 2015, **517**, 187–190.
- 4 R. Subbaraman, D. Tripkovic, K. C. Chang, D. Strmcnik, A. P. Paulikas, P. Hirunsit, M. Chan, J. Greeley, V. Stamenkovic and N. M. Markovic, *Nat. Mater.*, 2012, **11**, 550–557.

- 5 K. L. Zhou, Z. Wang, C. B. Han, X. Ke, C. Wang, Y. Jin, Q. Zhang, J. Liu, H. Wang and H. Yan, *Nat. Commun.*, 2021, **12**, 3783.
- 6 M. Zhong, W. Li, J. Chen, S. Ren, R. Qi, C. Wang and X. Lu, *Sep. Purif. Technol.*, 2023, **310**, 123164.
- 7 T. Xiong, Z. Zhu, Y. He, M. S. Balogun and Y. Huang, *Small Methods*, 2023, **7**, 2201472.
- 8 Y. Wang, D. Chen, J. Zhang, M. S. Balogun, P. Wang, Y. Tong and Y. Huang, *Adv. Funct. Mater.*, 2022, **32**, 2112738.
- 9 X. Lu, K.-h. Ye, S. Zhang, J. Zhang, J. Yang, Y. Huang and H. Ji, *Chem. Eng. J.*, 2022, **428**, 131027.
- 10 L. L. Feng, G. Yu, Y. Wu, G. D. Li, H. Li, Y. Sun, T. Asefa, W. Chen and X. Zou, *J. Am. Chem. Soc.*, 2015, **137**, 14023–14026.
- 11 W. Li, M. Li, C. Wang and X. Lu, *Sci. China: Mater.*, 2023, **66**, 1024–1032.
- 12 A. Kumar, X. Liu, J. Lee, B. Debnath, A. R. Jadhav, X. Shao, V. Q. Bui, Y. Hwang, Y. Liu, M. G. Kim and H. Lee, *Energy Environ. Sci.*, 2021, **14**, 6494–6505.
- 13 H. Xu, Y. Liao, Z. Gao, Y. Qing, Y. Wu and L. Xia, *J. Mater. Chem. A*, 2021, **9**, 3418–3426.
- 14 W. Chen, C. Xie, Y. Wang, Y. Zou, C.-L. Dong, Y.-C. Huang, Z. Xiao, Z. Wei, S. Du, C. Chen, B. Zhou, J. Ma and S. Wang, *Chem*, 2020, **6**, 2974–2993.
- 15 W. Chen, L. Xu, X. Zhu, Y. C. Huang, W. Zhou, D. Wang, Y. Zhou, S. Du, Q. Li, C. Xie, L. Tao, C. L. Dong, J. Liu, Y. Wang, R. Chen, H. Su, C. Chen, Y. Zou, Y. Li, Q. Liu and S. Wang, *Angew. Chem., Int. Ed.*, 2021, **60**, 7297–7307.
- 16 C. Chen, X. Zhu, X. Wen, Y. Zhou, L. Zhou, H. Li, L. Tao, Q. Li, S. Du, T. Liu, D. Yan, C. Xie, Y. Zou, Y. Wang, R. Chen, J. Huo, Y. Li, J. Cheng, H. Su, X. Zhao, W. Cheng, Q. Liu, H. Lin, J. Luo, J. Chen, M. Dong, K. Cheng, C. Li and S. Wang, *Nat. Chem.*, 2020, **12**, 717–724.
- 17 G. Soloveichik, *Nat. Catal.*, 2019, **2**, 377–380.
- 18 X. Xu, H. Ullah, M. Humayun, L. Li, X. Zhang, M. Bououdina, D. P. Debecker, K. Huo, D. Wang and C. Wang, *Adv. Funct. Mater.*, 2023, **33**, 2303986.
- 19 S.-K. Geng, Y. Zheng, S.-Q. Li, H. Su, X. Zhao, J. Hu, H.-B. Shu, M. Jaroniec, P. Chen, Q.-H. Liu and S.-Z. Qiao, *Nat. Energy*, 2021, **6**, 904–912.
- 20 F. Guo, K. Ye, M. Du, X. Huang, K. Cheng, G. Wang and D. Cao, *Electrochim. Acta*, 2016, **210**, 474–482.
- 21 P. Li, W. Li, Y. Huang, Q. Huang, F. Li and S. Tian, *Small*, 2023, **19**, 2305585.
- 22 H. Qin, Y. Ye, J. Li, W. Jia, S. Zheng, X. Cao, G. Lin and L. Jiao, *Adv. Funct. Mater.*, 2023, **33**, 2209698.
- 23 K. Zhang, S. Wang, X. Li, H. Li and Y. Ni, *Small*, 2023, **19**, 2300959.
- 24 P. Li, W. Li, Y. Huang, Q. Huang and S. Tian, *Small*, 2023, **19**, 2300725.
- 25 M. Ranjani, N. Senthilkumar, G. Gnana kumar and A. Manthiram, *J. Mater. Chem. A*, 2018, **6**, 23019–23027.
- 26 N. Senthilkumar, G. Gnana kumar and A. Manthiram, *Adv. Energy Mater.*, 2017, **8**, 1702207.
- 27 S. Huang, Q. Zhang, P. Xin, J. Zhang, Q. Chen, J. Fu, Z. Jin, Q. Wang and Z. Hu, *Small*, 2022, **18**, 2106841.
- 28 M. Zhong, W. Li, C. Wang and X. Lu, *Appl. Surf. Sci.*, 2022, **575**, 151708.
- 29 N. Chen, Y.-X. Du, G. Zhang, W.-T. Lu and F.-F. Cao, *Nano Energy*, 2021, **81**, 105605.
- 30 R.-Q. Li, Q. Liu, Y. Zhou, M. Lu, J. Hou, K. Qu, Y. Zhu and O. Fontaine, *J. Mater. Chem. A*, 2021, **9**, 4159–4166.
- 31 Y. Dong, Y. Wu, X. Wang, H. Wang, J. Ren, P. Wang, L. Pan, G. Wang and R. Wang, *Nanoscale*, 2023, **15**, 1813–1823.
- 32 Y. Ding, Y. Li, Y. Xue, B. Miao, S. Li, Y. Jiang, X. Liu and Y. Chen, *Nanoscale*, 2019, **11**, 1058–1064.
- 33 B. Zhu, Z. Liang and R. Zou, *Small*, 2020, **16**, 1906133.
- 34 C. Liu, X. R. Shi, K. Yue, P. Wang, K. Zhan, X. Wang, B. Y. Xia and Y. Yan, *Adv. Mater.*, 2023, **35**, 2211177.
- 35 Y. Sun, H. Shin, F. Wang, B. Tian, C. W. Chiang, S. Liu, X. Li, Y. Wang, L. Tang, W. A. I. Goddard and M. Ding, *J. Am. Chem. Soc.*, 2022, **144**, 15185–15192.
- 36 J. Zhang, J. Dang, X. Zhu, J. Ma, M. Ouyang and F. Yang, *Appl. Catal., B*, 2023, **325**, 122296.
- 37 Z. Yin, R. He, Y. Zhang, L. Feng, X. Wu, T. Wågberg and G. Hu, *J. Energy Chem.*, 2022, **69**, 585–592.
- 38 Y. J. Lee and S. K. Park, *Small*, 2022, **18**, 2200586.
- 39 A. Pei, R. Xie, Y. Zhang, Y. Feng, W. Wang, S. Zhang, Z. Huang, L. Zhu, G. Chai, Z. Yang, Q. Gao, H. Ye, C. Shang, B. H. Chen and Z. Guo, *Energy Environ. Sci.*, 2023, **16**, 1035–1048.
- 40 B. Zhou, Y. Li, Y. Zou, W. Chen, W. Zhou, M. Song, Y. Wu, Y. Lu, J. Liu, Y. Wang and S. Wang, *Angew. Chem., Int. Ed.*, 2021, **60**, 22908–22914.
- 41 Z. Liu, J. Li, S. Xue, S. Zhou, K. Qu, Y. Li and W. Cai, *J. Energy Chem.*, 2020, **47**, 317–323.
- 42 H. Zhang, F. Wan, X. Li, X. Chen, S. Xiong and B. Xi, *Adv. Funct. Mater.*, 2023, **33**, 2306340.
- 43 C. Hu, Y. Hu, C. Fan, L. Yang, Y. Zhang, H. Li and W. Xie, *Angew. Chem., Int. Ed.*, 2021, **60**, 19774–19778.
- 44 D. Y. Wei, M. F. Yue, S. N. Qin, S. Zhang, Y. F. Wu, G. Y. Xu, H. Zhang, Z. Q. Tian and J. F. Li, *J. Am. Chem. Soc.*, 2021, **143**, 15635–15643.
- 45 S. Lin, H. Ze, X. G. Zhang, Y. J. Zhang, J. Song, H. Zhang, H. L. Zhong, Z. L. Yang, C. Yang, J. F. Li and Z. Zhu, *Angew. Chem., Int. Ed.*, 2022, **61**, e202203511.
- 46 A. Mosallanezhad, C. Wei, P. Ahmadian Koudakan, Y. Fang, S. Niu, Z. Bian, B. Liu, T. Huang, H. Pan and G. Wang, *Appl. Catal., B*, 2022, **315**, 121534.
- 47 S. Vijayapradeep, N. Logeshwaran, S. Ramakrishnan, A. Rhan Kim, P. Sampath, D. Hwan Kim and D. Jin Yoo, *Chem. Eng. J.*, 2023, **473**, 145348.
- 48 W. Zhang, Q. Jia, H. Liang, L. Cui, D. Wei and J. Liu, *Chem. Eng. J.*, 2020, **396**, 125315.
- 49 T. Wang, L. Miao, S. Zheng, H. Qin, X. Cao, L. Yang and L. Jiao, *ACS Catal.*, 2023, **13**, 4091–4100.
- 50 K. L. Zhou, C. Wang, Z. Wang, C. B. Han, Q. Zhang, X. Ke, J. Liu and H. Wang, *Energy Environ. Sci.*, 2020, **13**, 3082–3092.
- 51 Y. Tian, M. Wen, A. Huang, Q. Wu, Z. Wang, Q. Zhu, T. Zhou and Y. Fu, *Small*, 2023, **19**, 2207569.
- 52 B. Tang, X. Yang, Z. Kang and L. Feng, *Appl. Catal., B*, 2020, **278**, 119281.

- 53 M. Li, H. Wang, W. Zhu, W. Li, C. Wang and X. Lu, *Adv. Sci.*, 2020, **7**, 1901833.
- 54 Z. Xu, Q. Chen, Q. Chen, P. Wang, J. Wang, C. Guo, X. Qiu, X. Han and J. Hao, *J. Mater. Chem. A*, 2022, **10**, 24137–24146.
- 55 L. Sha, K. Ye, J. Yin, K. Zhu, K. Cheng, J. Yan, G. Wang and D. Cao, *Chem. Eng. J.*, 2020, **381**, 122603.
- 56 V. Vedharathinam and G. G. Botte, *Electrochim. Acta*, 2012, **81**, 292–300.
- 57 A. V. Munde, B. B. Mulik, P. P. Chavan and B. R. Sathe, *Electrochim. Acta*, 2020, **349**, 136386.
- 58 D. Voiry, M. Chhowalla, Y. Gogotsi, N. A. Kotov, Y. Li, R. M. Penner, R. E. Schaak and P. S. Weiss, *ACS Nano*, 2018, **12**, 9635–9638.
- 59 C. Liu, H. Ma, M. Yuan, Z. Yu, J. Li, K. Shi, Z. Liang, Y. Yang, T. Zhu, G. Sun, H. Li and S. Ma, *Electrochim. Acta*, 2018, **286**, 195–204.
- 60 X. Fu, R. Shi, S. Jiao, M. Li and Q. Li, *J. Energy Chem.*, 2022, **70**, 129–153.
- 61 S. W. Tatarchuk, J. J. Medvedev, F. Li, Y. Tobolovskaya and A. Klinkova, *Angew. Chem., Int. Ed.*, 2022, **61**, e202209839.
- 62 R. Li, H. Xu, P. Yang, D. Wang, Y. Li, L. Xiao, X. Lu, B. Wang, J. Zhang and M. An, *Nano-Micro Lett.*, 2021, **13**, 120.
- 63 Z. Gao, Y. Wang, L. Xu, Q. Tao, X. Wang, Z. Zhou, Y. Luo, J. Yu and Y. Huang, *Chem. Eng. J.*, 2022, **433**, 133515.
- 64 Z.-Y. Yu, C.-C. Lang, M.-R. Gao, Y. Chen, Q.-Q. Fu, Y. Duan and S.-H. Yu, *Energy Environ. Sci.*, 2018, **11**, 1890–1897.
- 65 Q. Zhang, F. M. D. Kazim, S. Ma, K. Qu, M. Li, Y. Wang, H. Hu, W. Cai and Z. Yang, *Appl. Catal., B*, 2021, **280**, 119436.
- 66 M. Zhong, J. Yang, M. Xu, S. Ren, X. Chen, C. Wang, M. Gao and X. Lu, *Small*, 2023, 2304782, DOI: [10.1002/sml.202304782](https://doi.org/10.1002/sml.202304782).
- 67 L. Sha, T. Liu, K. Ye, K. Zhu, J. Yan, J. Yin, G. Wang and D. Cao, *J. Mater. Chem. A*, 2020, **8**, 18055–18063.
- 68 S. Chen, J. Duan, A. Vasileff and S. Z. Qiao, *Angew. Chem., Int. Ed.*, 2016, **55**, 3804–3808.
- 69 H. Xu, K. Ye, K. Zhu, Y. Gao, J. Yin, J. Yan, G. Wang and D. Cao, *ACS Sustainable Chem. Eng.*, 2020, **8**, 16037–16045.
- 70 Y. Ye, Y. Gan, R. Cai, X. Dai, X. Yin, F. Nie, Z. Ren, B. Wu, Y. Cao and X. Zhang, *J. Alloys Compd.*, 2022, **921**, 166145.
- 71 L. Zhang, T. Wang, H. Wu, H. Wang and F. Wang, *J. Alloys Compd.*, 2022, **918**, 165564.
- 72 I. M. A. Mohamed, P. Kanagaraj, A. S. Yasin, W. Iqbal and C. Liu, *J. Alloys Compd.*, 2020, **816**, 152513.
- 73 Y. Yang, J. Kim, H. Jo, A. Seong, M. Lee, H.-K. Min, M.-G. Seo, Y. Choi and G. Kim, *J. Mater. Chem. A*, 2021, **9**, 11571–11579.
- 74 C. Sanchez, F. J. Espinos, A. Barjola, J. Escorihuela and V. Compan, *Polymers*, 2022, **14**, 4500.